Science Advances
AAAS

Supplementary Materials for

Reconfigurable 4D printing via mechanically robust covalent adaptable network shape memory polymer

Honggeng Li *et al.*

Corresponding author: Qi Ge, geq@sustech.edu.cn

The PDF file includes:

Sections S1 to S4
Figs. S1 to S25
Table S1
Legends for movies S1 to S12

Other Supplementary Material for this manuscript includes the following:

Movies S1 to S12

Supplementary Part 1. Thermomechanical properties of CAN-SMPs

Table S1. Comparison on processing methods and key thermomechanical properties of CAN-SMPs.

CAN SMPs (Dynamic Covalent bonds)	Processing Methods	Young's modulus (MPa)	T_{fix} (°C)	T_{trans} (°C)	ε_b at T_p (%)	R_f (%)	R_r (%)	R_{ret} (%)	Ref.
Crystalline SMP									
PETMA-PCLDA (Transesterification)	Molding and UV Curing	N/R	0	55 (T_{crys})	750-1100 (70°C)	98	98	~100	[27]
PETMA-PCLDA-PPDLDA (Transesterification)	Molding and UV Curing	N/R	-20	13 (T_{crys})	N/R	N/R	~98.7	N/R	[28]
PETMA -PCLDA-PPDLDA (Transesterification)	DLP (at 70°C, in 400 wt% toluene solvent)	100 (25°C)	-20	41 (T_{crys})	1200 (25°C)	N/R	N/R	N/R	[29]
PCL-PEG2000-TBEA-HDI (Transesterification and Transcarbamoylation)	Thermal Curing (50ºC overnight)	N/R	0	~53 (T_{crys})	~140 (50°C)	94	94	~100	[30]
PHMDI-PCLdiol-PSA （U1.7-PCL-PSA6-Zn4）	FDM	59.1 ± 14 (25°C)	-50	-19 (T_{crys})	26.6 ±2	N/R	N/R	N/R	[31]
PCL-PHMD-HDI (Transesterification)	Thermal Curing (60°C for 2 h)	~0.3 (37°C)	0	~37 (T_{crys})	1130%	97%	97%	~100	[32]
Crystalline SMP with thermo- and photo-reversible bonds (Transesterification)	Thermal Curing (80°C for 48 h)	90.6 (0°C)	0	~50 (T_{crys})	~600 (80°C)	N/R	~96.6	~100	[33]
PEG-IPDI-HEDS (Dynamic Disulfide Bonds)	Thermal Curing (50°C for 8 h)	~100 (25°C)	0	32.84 (T_{crys})	N/R	99	98	N/R	[34]
PEG200-GLY-HDI (Transcarbamoylation)	Thermal Curing (60°C for 2 h)	N/R	0	41 (T_{crys})	N/R	98	99	N/R	[35]
N-hydroxyethylacrylamide-PEGDA (Transesterification)	Molding and UV Curing	~58.5 (37°C)	0 or -20	~32 (T_{crys})	N/R	N/R	N/R	N/R	[36]
HDT-HDDA (Transesterification)	Thermal Curing (50ºC for 24 h)	N/R	0	25.16 (T_{crys})	~100	92	99	85	[37]
PTME-UpyA-BADA (Ureidopyrimidinone Supramolecular)	DLP (at 50°C)	<6 (25°C)	-20	6 (T_{crys})	200-400 (25°C)	N/R	N/R	N/R	[38]
PEG2000-TBEA-GLY-HDI (Urethane and Hindered Urea)	Thermal Curing (60°C for 4 h)	0.25-1.17 (25°C)	0	37 (T_{crys})	~520 (25°C)	95	95	N/R	[39]
PAH/PCL Re-SMEC (Anhydride-Based)	UV Curing (1 h) and Thermal Curing (70°C for 1 h)	<10 (25°C)	-40	30.3 (T_{crys})	150-200	87	78-93	N/R	[40]
Amorphous SMP									
MMA-DCL (Thiocarbamate Bonds)	DLP	500-1200 (25°C)	20	83 (T_g)	~10	~98	~97	N/R	[41]
EGPEA-IBOA-MEFB-HPASi: IEMSi3 (Dynamic Imine Bonds)	DLP	57-602 (25°C)	0	57-66 (T_g)	39.3	97.5	91.4	84.3	[42]
MRC-SMP (Transesterification)	**DLP**	**870-1420 (25°C)**	**25**	**75-79 (T_g)**	**1640 (105°C)**	**99.9**	**99.7**	**~100**	**This work**

In table S1, T_{fix} is the temperature used to fix the programmed shape of a SMP sample. ε_b at T_p is the failure strain of a SMP sample at programming temperature (T_p). T_{trans} is the transition temperature of SMP: for crystalline SMP, T_{trans} is the crystallization temperature (T_{crys}); for amorphous SMP, T_{trans} is the glass transition temperature (T_g). R_f refers to the shape fixing ratio of SMP in the shape memory cycle. R_r refers to the shape recovery ratio of SMP in the shape memory cycle. R_{ret} refers to the shape retention ratio of reconfiguration. Fig. S1-S3 show the failure strain at programming temperature, modulus variation range, and operation temperature range of different CAN-SMPs. Fig. S4 and S5 provide the details on how to calculate R_f, R_r, and R_{ret}. N/R in the table means no report.
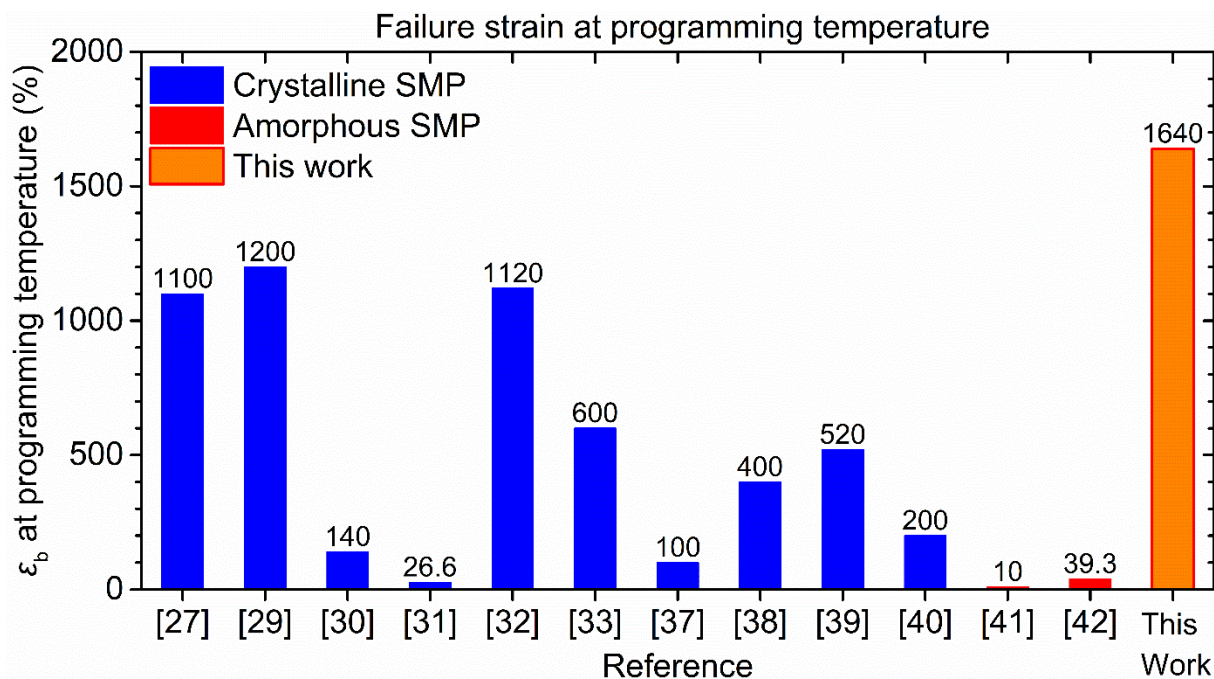
Fig. S1. Comparison on the failure strain at programming temperature of different CAN-SMPs.
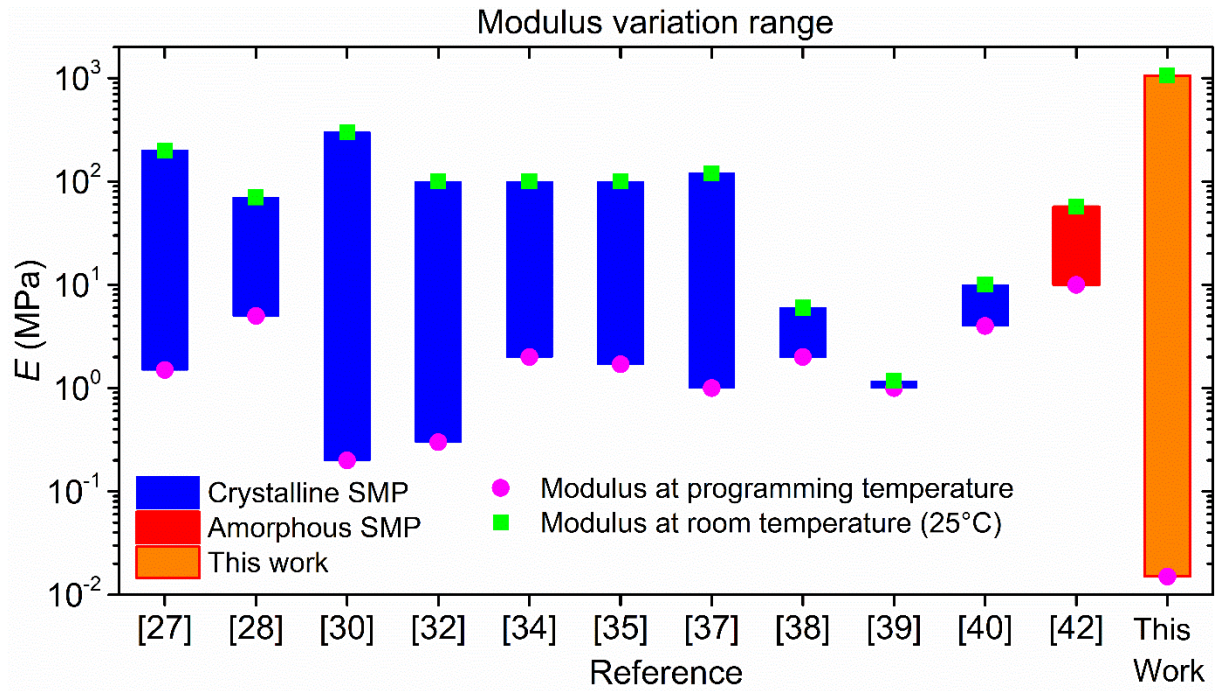
Fig. S2. Comparison on the modulus variation range of different CAN-SMPs.
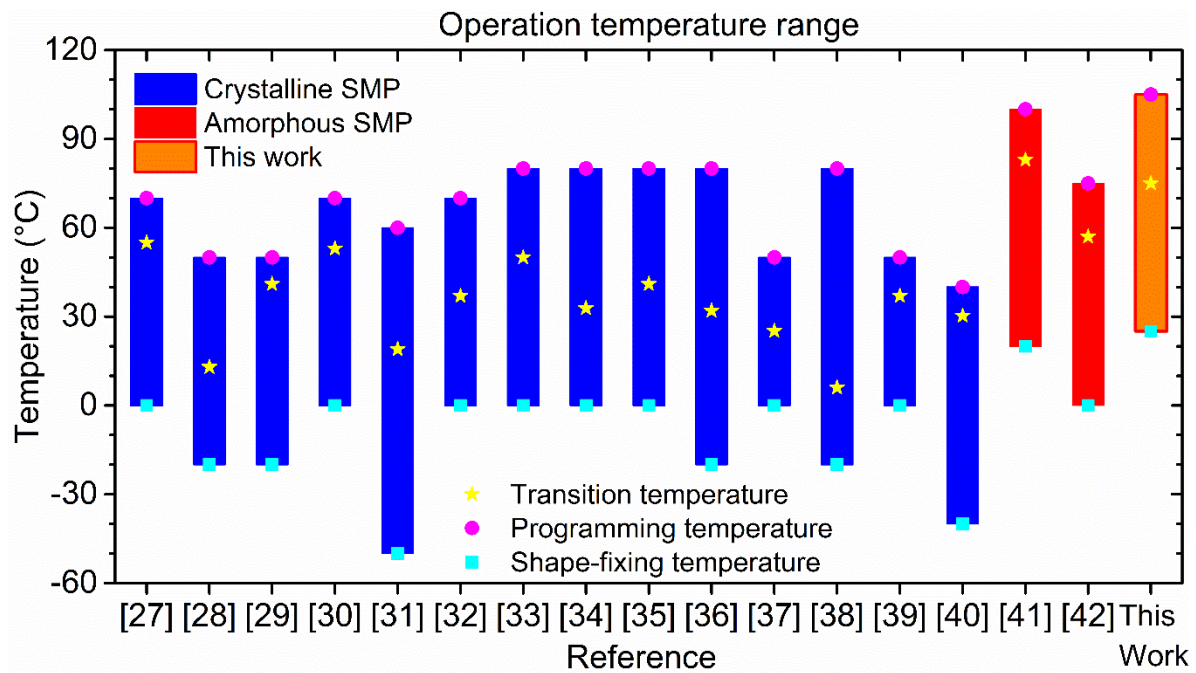

Fig. S3. Comparison on the operation temperature range of different CAN-SMPs.

Fig. S4 presents the result from a typical shape memory cyclic test for calculating R_f and R_r. At Step 1, an MRC-SMP sample is stretched to ε_p ($\varepsilon_p = 100\%$ in this work) at a constant strain rate (0.001 s^{-1}) at T_p (i.e., $T_g + 30°C$). At Step 2, the sample is cooled to 25°C with a cooling rate of 2.5°C/min and held at 25°C 2 mins while it is kept stretched. At Step 3, the external load is suddenly released at 25°C, and the temporary fixed strain ε_u can be measured. At step 4, the sample is heated to T_p at the heating rate of 2.5°C/min and held at T_p for 1 hour where the recovery strain ε_r is measured. Based on the above measured quantities, we calculate the shape fixing ratio R_f and shape recovery ratio R_r using the following two formulas:

$$R_f = 100\% \times \varepsilon_u / \varepsilon_p \text{ , and } R_r = 100\% \times (\varepsilon_u - \varepsilon_r)/\varepsilon_u \qquad (1)$$
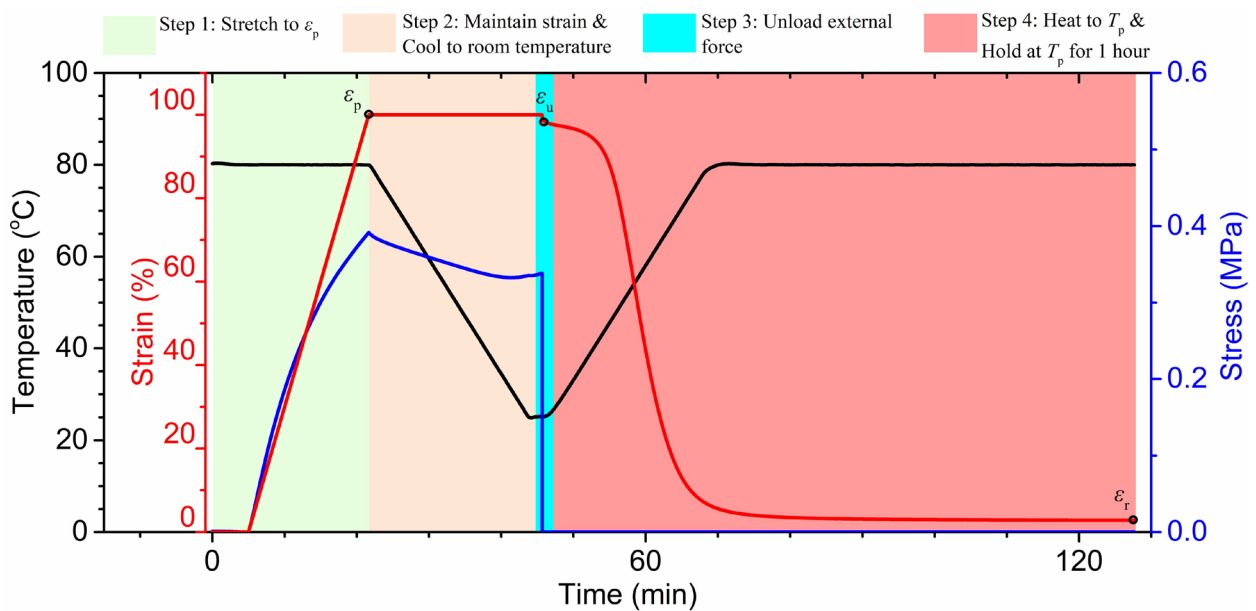

Fig. S4. Schematic diagram of a shape memory cyclic test for calculating shape fixing ratio and shape recovery ratio.

Fig. S5 presents the result from a typical stress relaxation experiment for calculating R_{ret}. The stress relaxation experiment was tested on a DMA analyzer (Q850 DMA, TA Instruments) at the reconfiguration temperature (150°C, in this work). First, the sample is quickly stretched by ε_{load} (ε_{load} = 100%) under the stress σ_0. Then, the deformation is maintained at ε_{load} for 30 mins and the stress $\sigma(t)$ is gradually relaxed. Then, the stress is relaxed, and the residual strain after stress relaxation ε_{relax} can be measured. We can calculate the shape retention ratio as

$$R_{ret} = 100\% \times \varepsilon_{relax} / \varepsilon_{load} \tag{2}$$

When the shape is completely reconfigured (stress is completely relaxed), shape retention ratio is 100%.
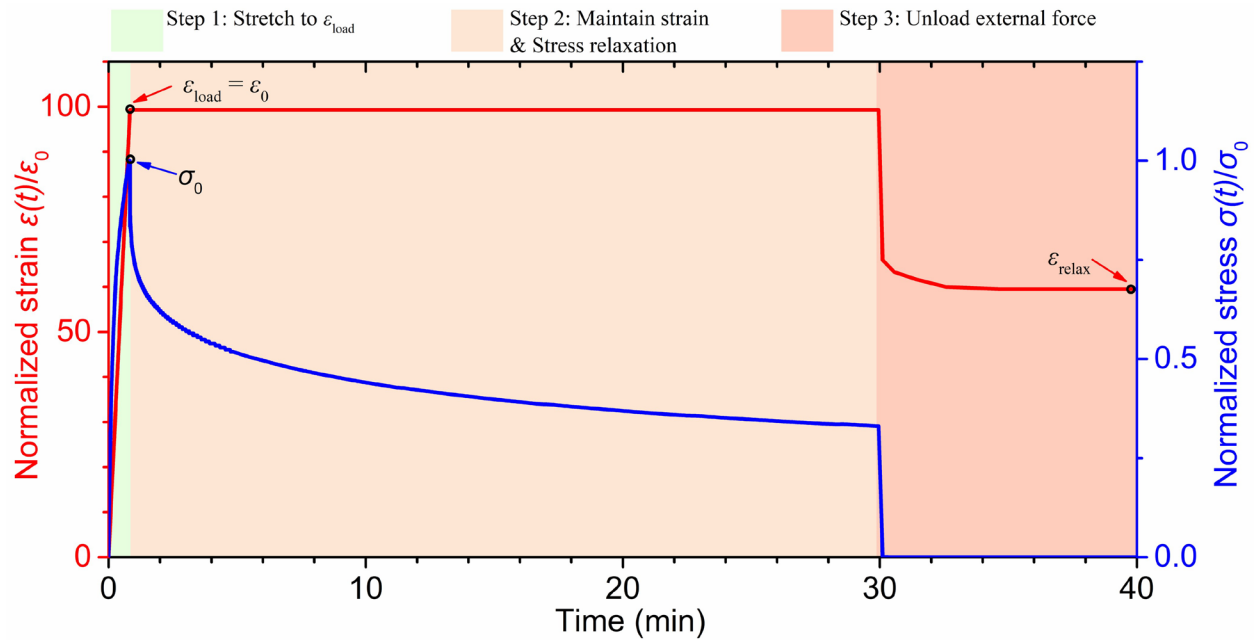

Fig. S5. Schematic diagram of a stress relaxation test for calculating shape retention calculation.

Supplementary Part 2. Preparation and Thermomechanical Properties of MRC-SMP

Catalyzed by TBD, heat treatment activates ester bond exchange reactions in the MRC-SMP network, resulting in dynamic covalent crosslinks, thereby endowing the MRC-SMP network with reconfigurability. There are abundant dynamic ester bonds on the long chain of AUD, which can undergo BERs with the ester bonds on the side chains of IBoA-BA to form new cross-linking points in the MRC-SMP network (Fig. S6A). Transesterification may also occur between multiple AUD long chains (Fig. S6B). Large number of BERs between side chains and AUD cross-links, as well as between multiple AUD cross-links, enable the MRC-SMP network to achieve complete stress relaxation in a new shape after reconfiguration.
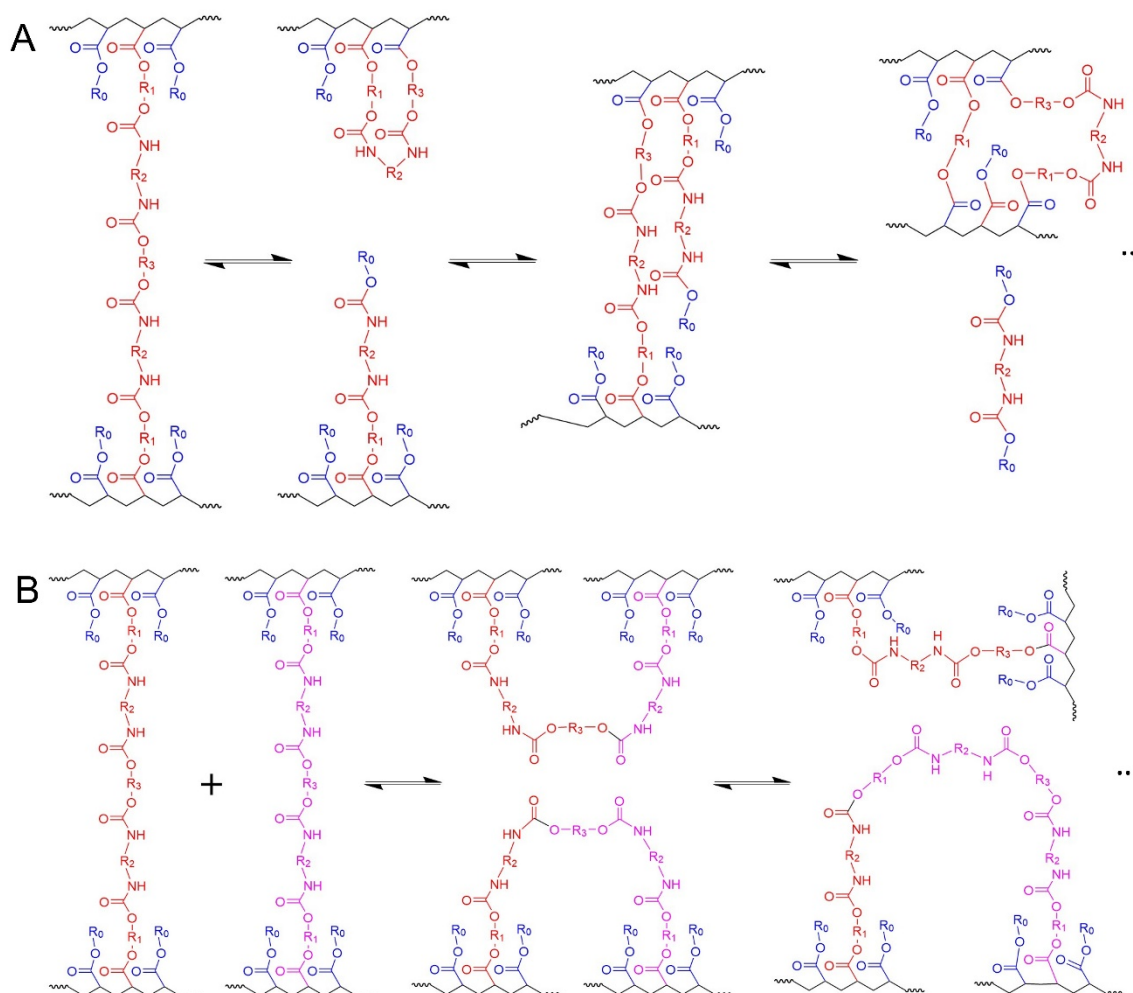

Fig. S6. BER process via transesterification in MRC-SMP networks. (**A**) Transesterification between AUD long chain and side chain of IBoA-BA. (**B**) Transesterification between multiple AUD long chains.

We investigated the effect of two monomer components on the T_g (Fig. S7). Photopolymerized IBoA-BA materials have typical thermoplastic properties, and the storage modulus decreases rapidly above T_g (Fig. S7A). The T_g of IBoA-BA materials increases with the increase of IBoA content (Fig. S7B). When IBoA reaches 75 wt.%, the glass-rubber transition region of IBoA-BA (that is, the peak region of Tan δ) is between room temperature (25°C) and transesterification reaction temperature (typical temperature is 130°C). Therefore, 75 wt.%: 25 wt.% (IBoA:BA) is an ideal ratio to achieve strong mechanical properties at room temperature and separation between programming temperature and bond exchange reaction temperature.
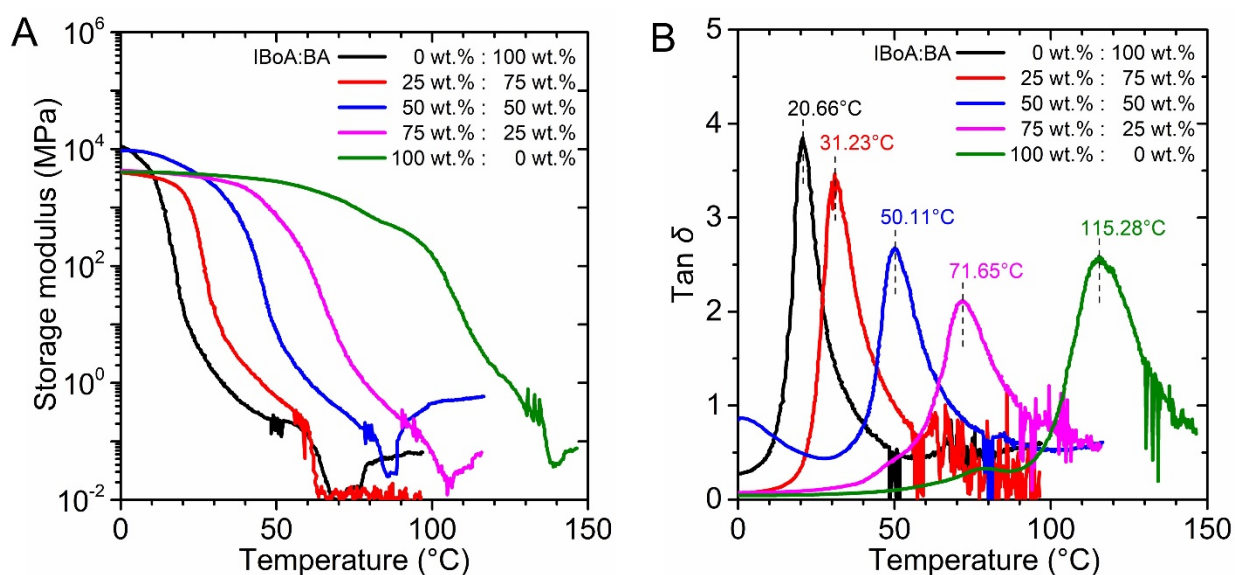

Fig. S7. Effect of IBoA-BA mixing ratio on the thermomechanical properties of IBoA-BA polymers. (**A**) Storage modulus curves. (**B**) Tan δ curves.

As shown in Fig. S8, we perform Gel Permeation Chromatography (GPC) test to determine the number-average molecular weight (M_n) and polymer dispersity index (PDI) of AUD crosslinker.
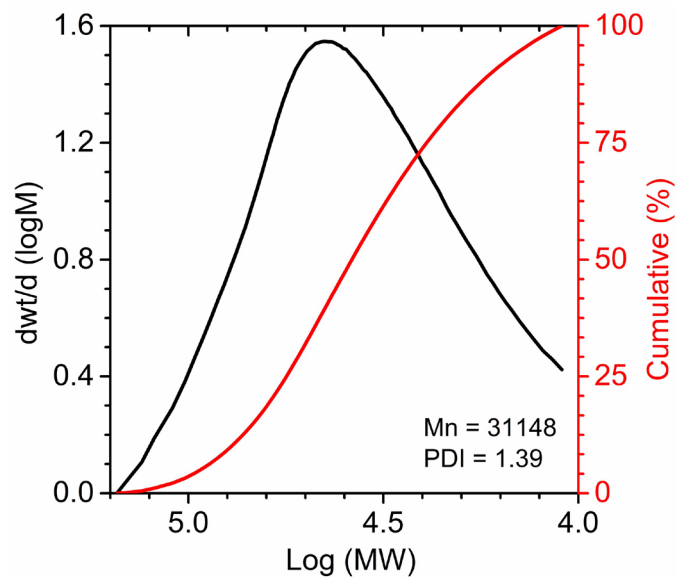

Fig. S8. Gel Permeation Chromatography test for AUD crosslinker.

To show that AUD is a better choice as crosslinker, we prepare the IBoA-BA-PEGDA SMP to compare thermomechanical performances of the two SMP systems. In the IBoA-BA-PEGDA SMP, Poly (ethylene glycol) diacrylate (PEGDA, $M_n = 575$) is used as crosslinker, and the molar fraction ($X_{crosslinker} = 0.00156$) of PEGDA is the same as that of AUD. The IBoA-BA-AUD SMP (MRC-SMP in this work) and IBoA-BA-PEGDA SMP have nearly the same T_g. As shown in Fig. S9A, we perform uniaxial tensile tests to investigate the stretchability of the IBoA-BA-PEDGA SMP at both programing temperature ($T_g + 30°C$) and BER temperature (150°C). The failure strains at $T_g + 30°C$ and 150°C are 351% and 271% respectively which are lower than that of the IBoA-BA-AUD SMP (Fig. S9B). Fig. S9C presents the stress relaxation test of the IBoA-BA-PEGDA SMP where the stress cannot be completely relaxed after 2 heating at 150°C, so that after unloading, only 82.42% of the applied strain is maintained ($R_{ret} = 82.42\%$). In contrast, as shown in Fig. S9D, the IBoA-BA-AUD SMP can completely relax all the applied stress after being heated at 150°C for 30 mins. Since all the stress is relaxed, after unloading, all the applied strain is maintained and the calculated shape retention ratio (R_{ret}) is 100%.
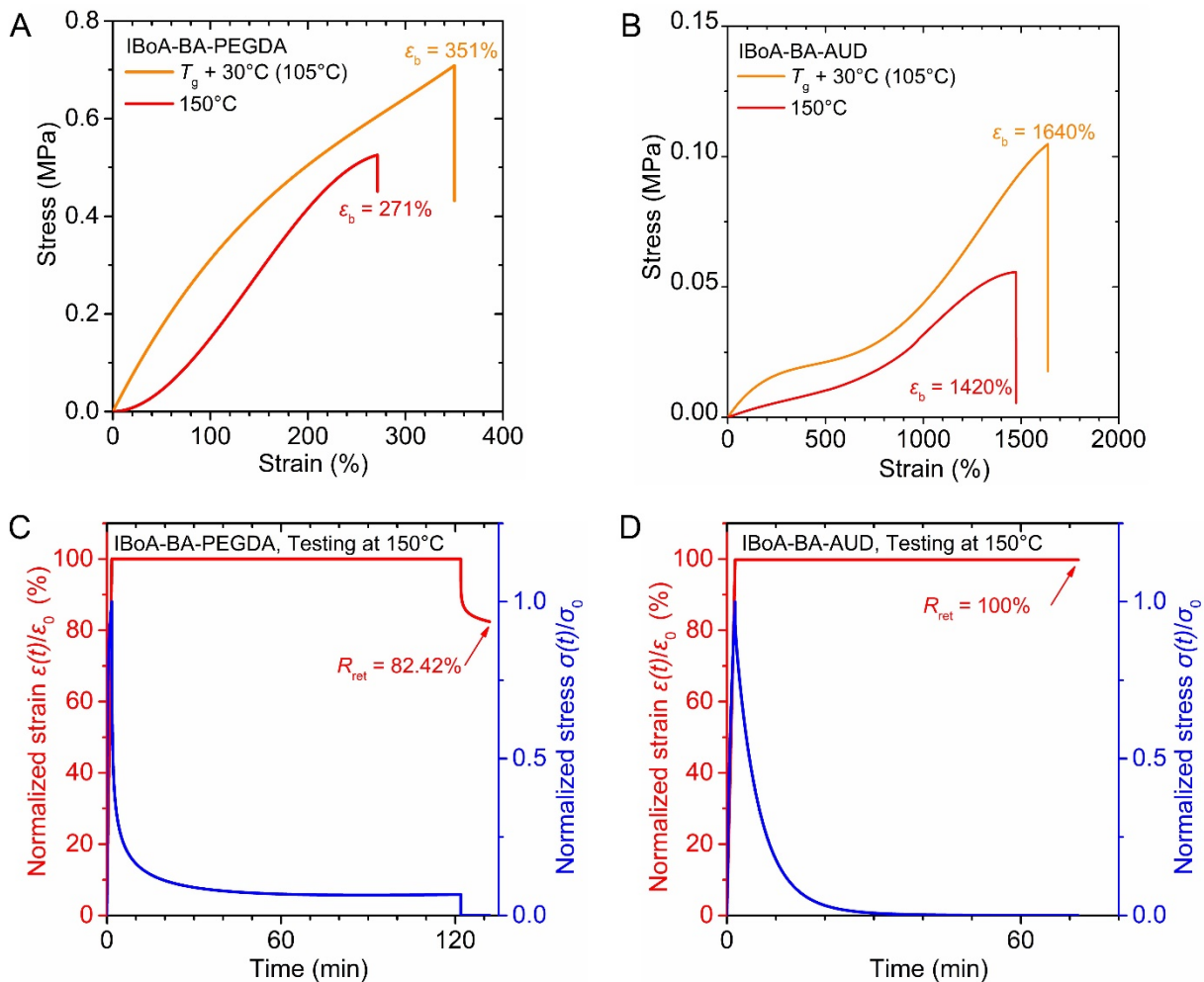
Fig. S9. Comparison on thermomechanical properties between IBoA-BA-AUD SMP and IBoA-BA-PEGDA SMP. (**A**) Stress-strain behaviors of IBoA-BA-PEGDA SMP. (**B**) Stress-strain behaviors of IBoA-BA-AUD SMP. (**C**) Stress relaxation test of IBoA-BA-PEGDA SMP at 150°C. (**D**) Stress relaxation test of IBoA-BA-AUD SMP at 150°C.

The AUD content has a notable impact on mechanical properties of MRC-SMPs at room temperature and programming temperature (105°C). The increases in the AUD content from 10 wt.% to 40 wt.% results in decrease in Young's modulus from 1.42 GPa to 0.87 GPa (Fig. S10A). Fig. S10B shows the increase in AUD content affect the Young's modulus of MRC-SMP samples at rubbery state (testing at 105°C) in the opposite way. As the AUD content increases, Young's modulus increases from 0.37 MPa to 0.91 MPa.
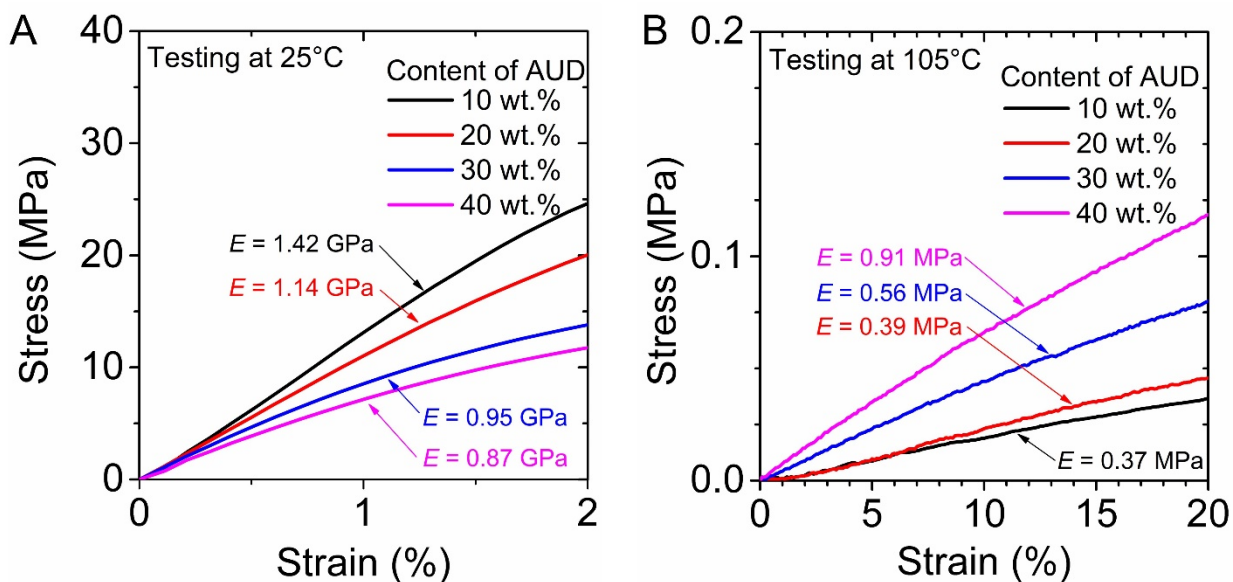

Fig. S10. Effect of AUD content on mechanical properties of MRC-SMPs. (A) At room temperature. (B) At programming temperature.

Stress relaxation experiments show that MRC-SMP with 1.5 wt.% TBD can relax completely within 17 minutes at 150°C, whereas MRC-SMP with 1.25 wt.% TBD takes 53 minutes (Fig. S11A). The stress relaxation of MRC-SMP with 2.0 wt.% TBD takes only 20 s (Fig. S11B).
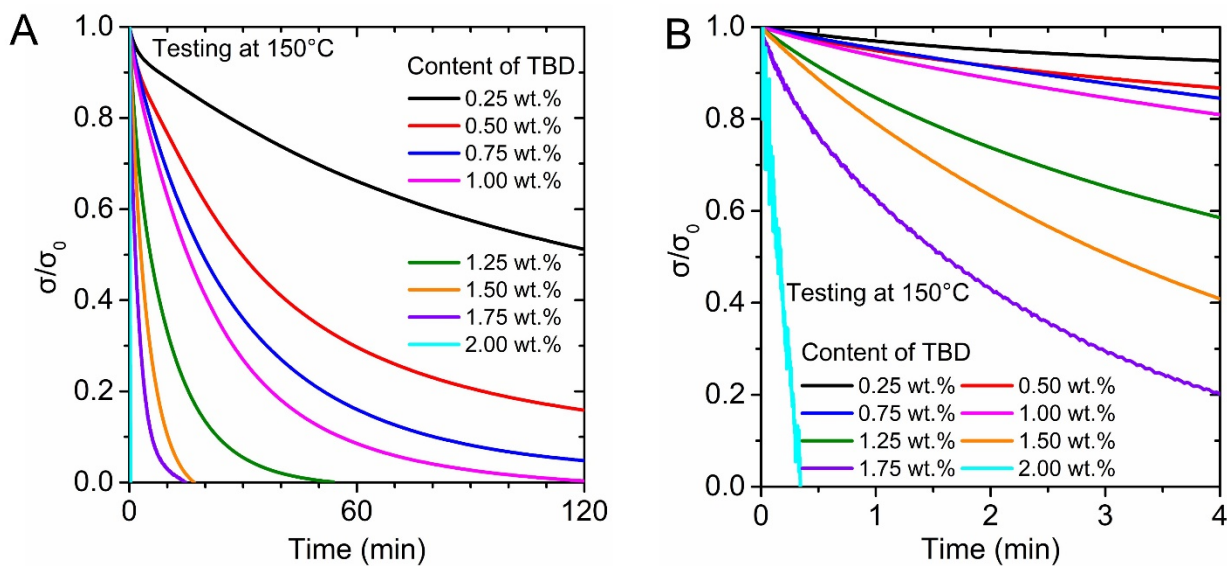

Fig. S11. Effect of TBD catalyst content on stress relaxation of MRC-SMP. (**A**) Stress relaxation curves within 2 hours. (**B**) Stress relaxation curves within 4 minutes.

The yield strength of MRC-SMPs decreases with the increase of TBD content, and the yield strength of MRC-SMP with 1.25 wt.% TBD was substantially lower than that of MRC-SMP with 1 wt.% TBD (Fig. S12A). As the TBD content increases, the modulus of MRC-SMPs decreases and the elongation at break increases until the TBD content reaches 1.5wt%. The modulus and elongation at break of MRC-SMP with 1.5 wt.% TBD are 1.06 GPa and 104%, respectively (Fig. S12B). Excessive TBD content reduces the elongation at break of MRC-SMPs. The elongation at break of MRC-SMP with 2.0 wt.% TBD is only 3% at room temperature.
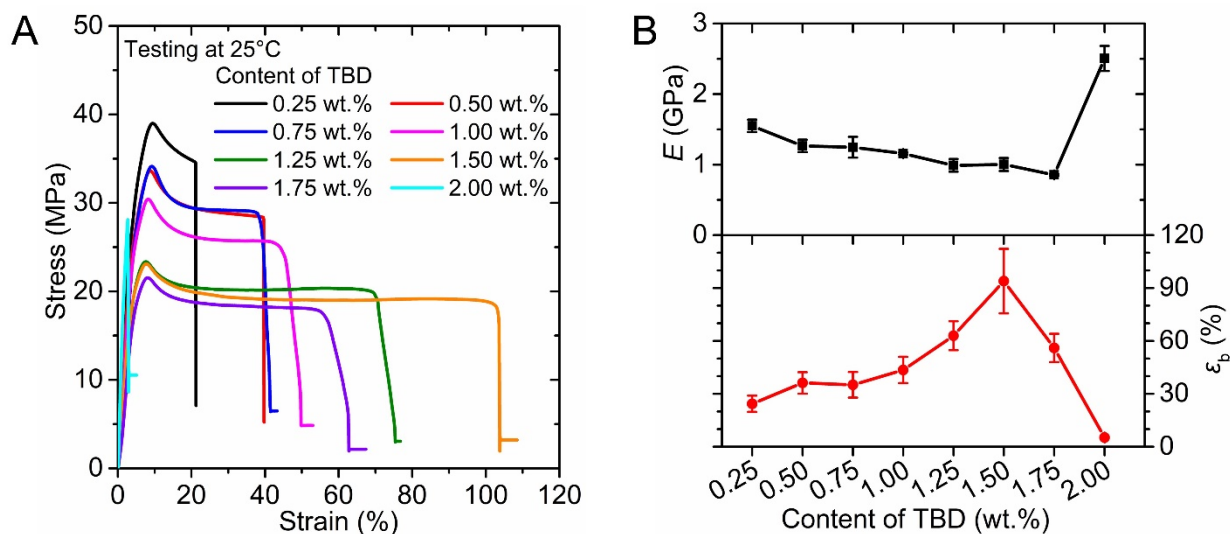

Fig. S12. Effect of catalyst content on mechanical properties of MRC-SMP at room temperature. (**A**) Tensile test results. (**B**) Young's Modulus and elongation at break.

Fig. S13 shows the shape memory cycles of an MRC-SMP sample (20 wt.% AUD and 1.5wt.% TBD) as prepared and after BER, respectively. The MRC-SMPs before and after BER all have excellent shape fixing ratios (as prepared: R_f = 99.88%; after BER: R_f = 99.88%) and shape recovery ratios (as prepared: R_r = 99.69%; after BER: R_r = 99.65%).
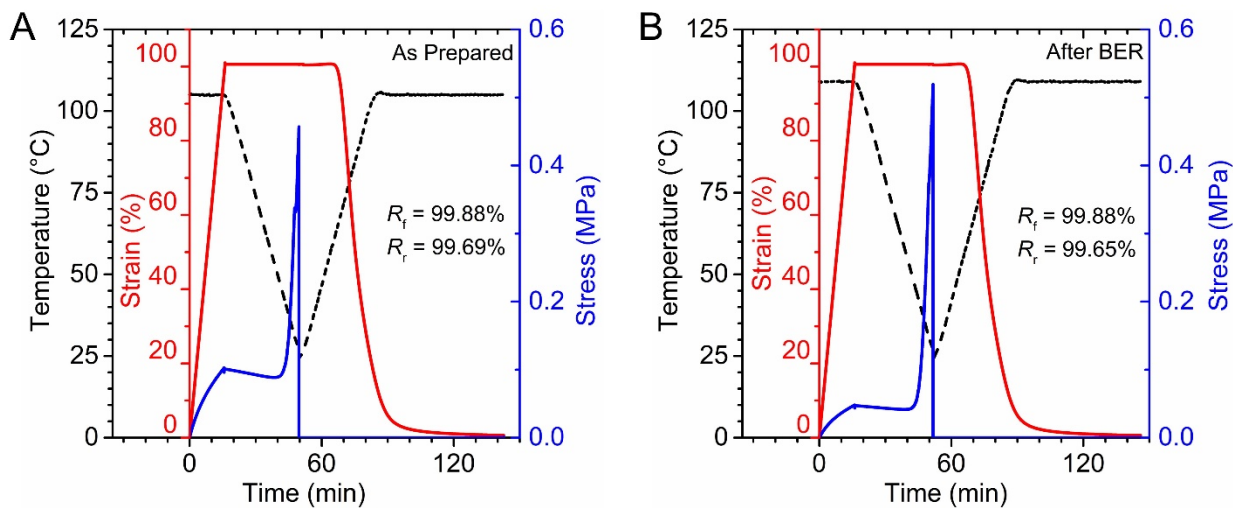

Fig. S13. Shape memory cycles of MRC-SMPs. (A) Shape memory cycle of MRC-SMP before BER (as prepared). **(B)** Shape memory cycle of MRC-SMP after BER (Heating 40 min).

In Fig. S14, we also investigate the thermomechanical behaviors of the MRC-SMP (20 wt.% AUD and 1.5wt.% TBD) at the programming temperature lower than 105°C (T_g + 30°C). Before the tests, all the MRC-SMP samples are thermally treated at 150°C for 40 mins to ensure the BERs proceed sufficiently. Fig. S14A compares the stress-strain behaviors of MRC-SMP samples at T_g (75°C), T_g + 15°C (90°C), and T_g + 30°C (105°C). The Young's modulus of the MRC-SMP increases to 0.015 MPa and 0.129 MPa when the programming temperature decreases from 105°C to 75°C. We also perform shape memory cyclic tests by setting the programming and recovery at 75°C and 90°C. As shown in Fig. S14B and S14C, the MRC-SMP samples all have excellent shape fixing ratio R_f and shape recovery ratio R_r when they are programmed at both 75°C and 90°C.
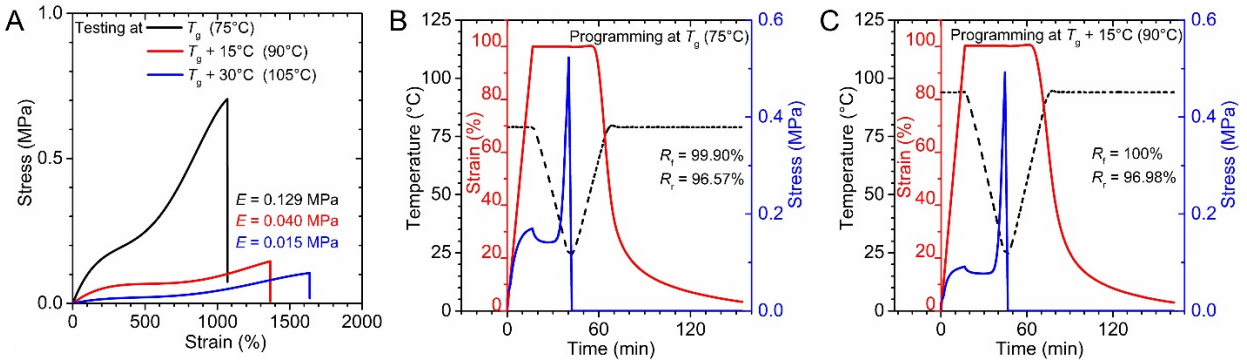

Fig. S14. Thermomechanical behaviors programmed at 75°C and 90°C of the MRC-SMP with 20 wt.% AUD. (A) Stress-strain behaviors at different temperatures. **(B)** Shape memory cycle with programming temperature at 75°C. **(C)** Shape memory cycle with programming temperature at 90°C.

Fig. S15A shows that the Young's modulus of the MRC-SMP samples at 105°C can be further increased from 0.015 MPa to 0.079 MPa by increasing the AUD content from 20 wt.% to 40 wt.%. Before the tests, all the MRC-SMP samples are thermally treated at 150°C for 40 mins to ensure the BERs proceed sufficiently. Fig. S15B and S15C further present the shape memory cycles for the MRC-SMP samples with 30 wt.% and 40 wt.% AUD contents. Although the Young's modulus at 105°C increased by increasing the AUD content, the MRC-SMP samples still exhibit excellent shape memory performances.
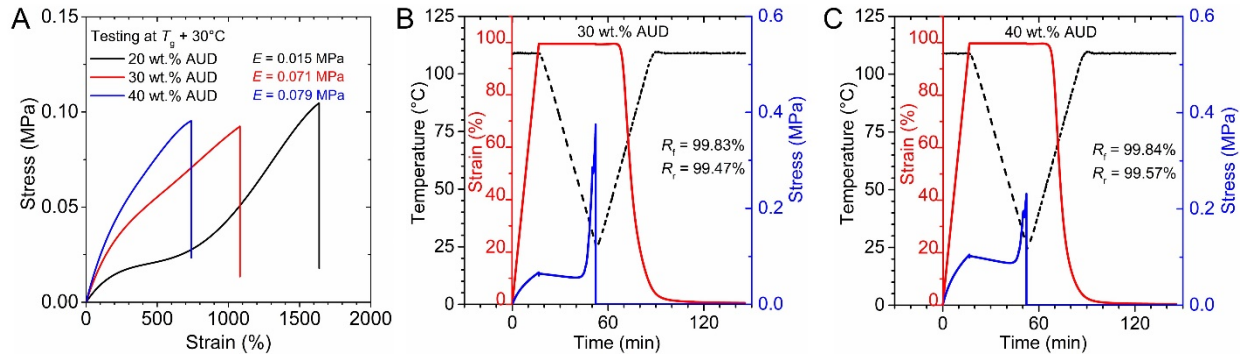

Fig. S15. Thermomechanical behaviors of the MRC-SMP sample with 30 wt.% and 40 wt.% AUD. (A) Stress-strain behaviors of the MRC-SMP sample with 30 wt.% and 40 wt.% AUD. **(B)** Shape memory cycle of the MRC-SMP sample with 30 wt.% AUD. **(C)** Shape memory cycle of the MRC-SMP sample with 40 wt.% AUD.

Supplementary Part 3. Reconfiguration and Welding of MRC-SMP

The strain rates and testing temperatures have notable impacts on mechanical properties of MRC-SMP above BER temperature. As shown in Fig. S16A, with strain rate ranging from 0.01/s to 10/s, the elongation at break of MRC-SMP decrease from 1471% to 449%, and the Young's modulus increase from 0.015 MPa to 0.035 MPa. Fig. S16b shows that under the same strain rate of 0.01/s, the MRC-SMP sample can be stretched more when the testing temperature is higher.
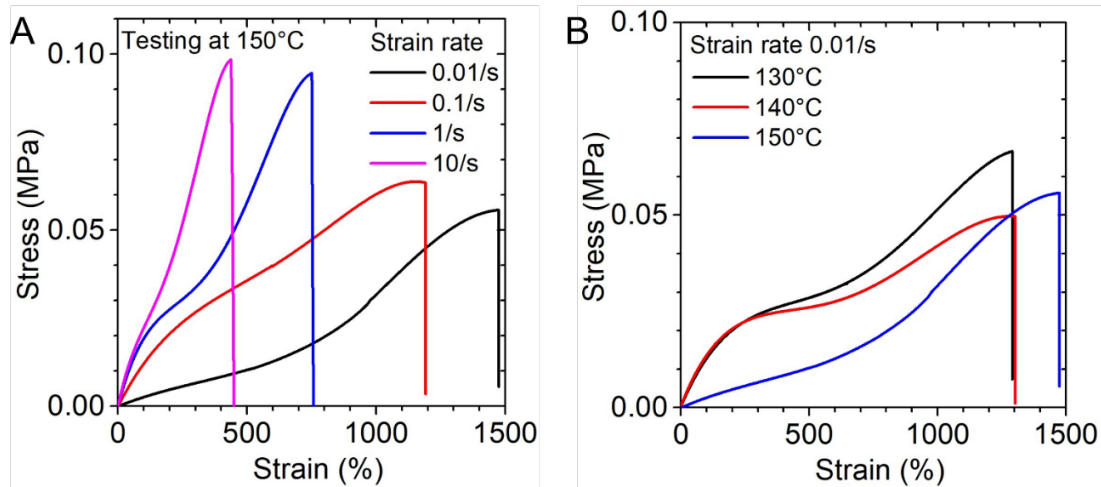

Fig. S16. Mechanical properties of MRC-SMP samples at different strain rates and testing temperatures. (**A**) Uniaxial tensile testing results of the MRC-SMP samples under different strain rates at 150°C. (**B**) Uniaxial tensile testing results of the MRC-SMP samples under 0.01/s strain rate at different testing temperatures.

Fig. S17A presents Small Angle X-ray Scattering (SAXS) patterns (the scattering intensity variation in the **q** space) of the five MRC-SMP samples after different thermomechanical treatments which are shown in Fig. 3(D to H) of the main text.

To quantitatively compare the scattering intensity variation of the five MRC-SMP samples, we calculate the integrated scattering intensity of an arbitrary arch adjacent the $\mathbf{q}_x$ axis (the Azimuth angle φ ranging from -15° to 15° around the $\mathbf{q}_x$ axis in Fig. S17B), and the $\mathbf{q}_y$ axis (the Azimuth angle φ ranging from 75° to 105° around the $\mathbf{q}_y$ axis in Fig. S17D):

$$I_{\mathbf{q}_x}^{\pm 15°} = \int_{-15°}^{15°} I(\mathbf{q}, \varphi) d\varphi, \tag{3}$$

$$I_{\mathbf{q}_y}^{\pm 15°} = \int_{75°}^{105°} I(\mathbf{q}, \varphi) d\varphi. \tag{4}$$

At the same location (the same q value ranging from 0.07 nm^{-1} to 0.4 nm^{-1}), $I_{\mathbf{q}_x}^{\pm 15°}$ of fresh sample stretched by 400% (3e) is higher than that of fresh sample (3h) (Fig. S17C), while $I_{\mathbf{q}_y}^{\pm 15°}$ of fresh sample stretched by 400% is lower than that of fresh sample (Fig. S17E). Compared with the fresh sample, $I_{\mathbf{q}_x}^{\pm 15°}$ and $I_{\mathbf{q}_y}^{\pm 15°}$ of the heat-treated sample are remarkably lower at the same location (Fig. S17C and S17E). The change in signal intensity caused by tensile deformation was also observed in heat-treated samples (comparing 3g and 3f in Fig. S17C and S17E). After heat treatment, $I_{\mathbf{q}_x}^{\pm 15°}$ and $I_{\mathbf{q}_y}^{\pm 15°}$ of the 400% stretched sample are remarkably reduced to lower than the values of the heat-treated sample (comparing 3h, 3g and 3f in Fig. S17C and S17E).

In order to quantitatively compare the scattering intensity at each Azimuth angle φ for the five MRC-SMP samples, we calculate the integrated scattering intensity along any arbitrary scattering vector **q** in the range of 0.07-0.2 nm^{-1} (q_1 to q_2) (Fig. S17F):

$$I_{q_1 \to q_2} = \int_{q_1}^{q_2} I(\mathbf{q}, \varphi) dq. \tag{5}$$

As shown in Fig. S17G, the scattering intensities of the fresh samples (3d) and heat-treated samples (3f) are independent on the Azimuth angle as they are undeformed and the polymer chains are randomly orientated. For the stretched fresh sample (3e) and the stretched heat-treated sample (3g), the scattering intensity is highly dependent on Azimuth angle where the highest intensity occurs at 0° and 180° ($\mathbf{q}_x$ axis), and the lowest intensity occurs at 90° and 270° ($\mathbf{q}_y$ axis). This indicates that

the stretching causes the polymer chains to be denser in *y*-direction. When the stretched sample is heat treated (3h), the scattering intensity becomes independent on the Azimuth angle again implying that the heat treatment induced BER rearranges the molecular topology from the stretching-oriented one to the randomly oriented one.
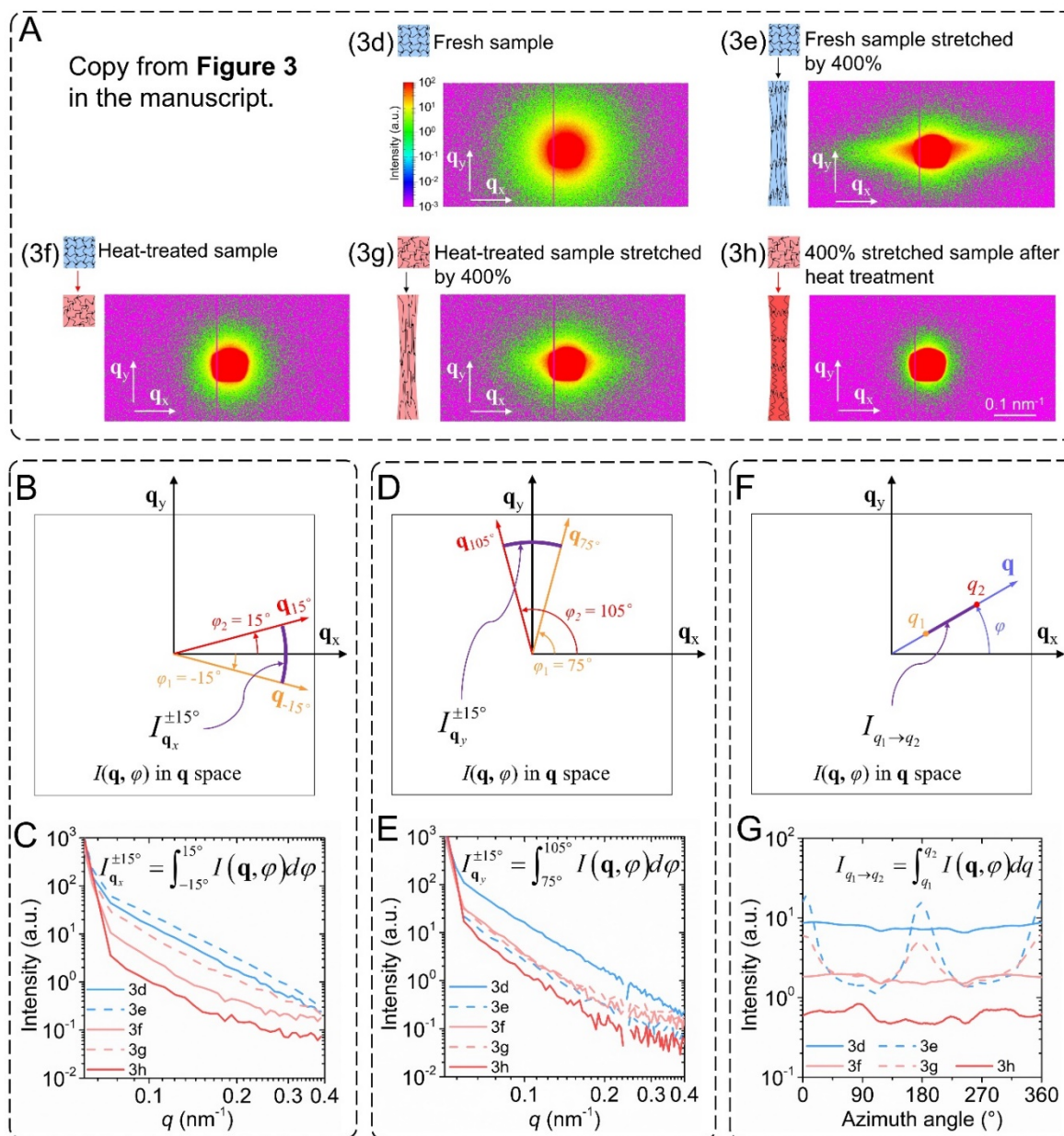

Fig. S17. Analyses of SAXS experiments of the MRC-SMPs under different thermomechanical treatments. (**A**) SAXS two-dimensional spectra. Copy from Figure 3 in the manuscript. (**B-E**) Scattering intensity variation of the five samples near $\mathbf{q}_x$ and $\mathbf{q}_y$ axes. (**F-G**) Scattering intensity variation at each azimuth angle.

Fig. S18 shows the shape fixing ratios and shape recovery ratios of the four SM cycles in the SM-reconfiguration cyclic experiment (Figure 3I in main text). The shape fixing ratios remained at ~100% in the four SM cycles. The shape recovery ratios of the first two cycles are ~95%. The shape recovery ratios of the last two cycles are ~90%.
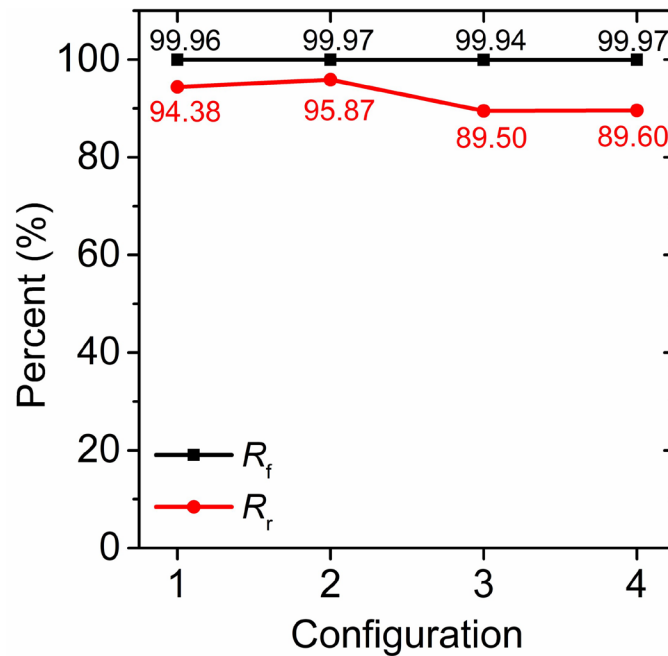

Fig. S18. Shape fixing ratios and shape recovery ratios of MRC-SMP in the SM-reconfiguration cyclic experiment.

Fig. S19 present design and manufacturing details on the samples for the lap shear experiments in Fig. 3K of the main text. Fig. S19A and S19B show the side-view profile dimensions of welded sample and control samples respectively. The width of all samples is 10 mm. Fig. S19C describes the manufacturing process of a welded sample: (i) printing two identical half parts; (ii) assembling two half parts; (iii) heating the assembled two parts at 150°C for 40 min to trigger BERs which weld the two half parts together. As shown in Fig. S19D, the control sample is directly 3D printed following by the heat treatment at 150°C for 40 min.
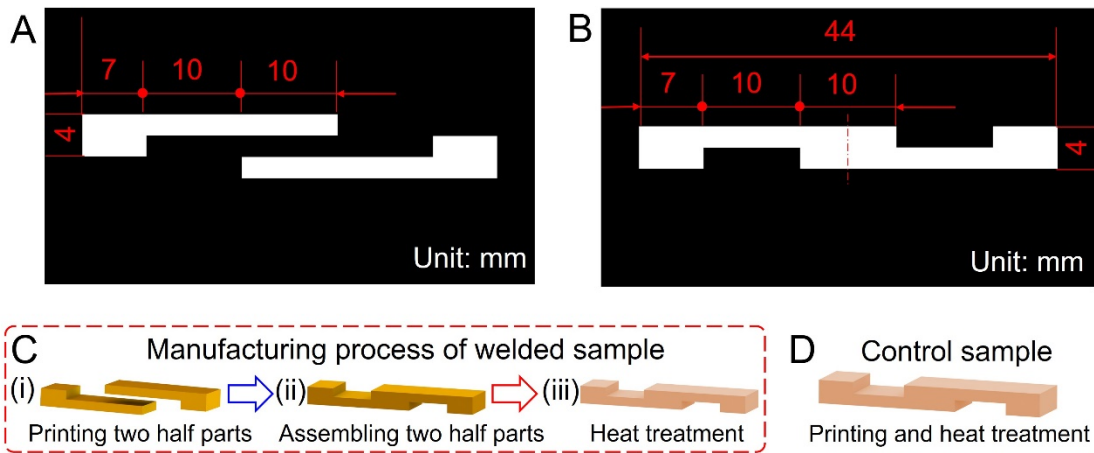

Fig. S19. Design and manufacturing details on the sample for lap shear experiment. (**A**) Side-view profile dimensions of the welded sample. (**B**) Side-view profile dimensions of control sample. (**C**) Manufacturing process of a welded sample. (**D**) Manufacturing process of a control sample.

Fig. S20 present design and manufacturing details on the dog-bone samples for uniaxial tensile tests to investigate interfacial bonding. Fig. S20A and S20B show the top-view profile dimensions of welded sample and control samples respectively. The thickness of all samples is 10 mm. Fig. S20C describes the manufacturing process of a welded sample: (i) printing two identical half parts; (ii) assembling two half parts; (iii) heating the assembled two parts at 150°C for 40 min to trigger BERs which weld the two half parts together. As shown in Fig. S20D, the control sample is directly 3D printed following by the heat treatment at 150°C for 40 min. Fig. S20E shows the stress-strain behaviors for both welded and control samples. The welded samples exhibit nearly the same mechanical response as the control samples, which indicates that BER causes molecular topological rearrangement to propagate across the boundary, and leads two separate parts to

chemically bonded to form an intact part. Fig. S20F shows that the welded sample is not fractured at the welded interface indicating that BER leads to a strong interfacial bonding between two separate parts.
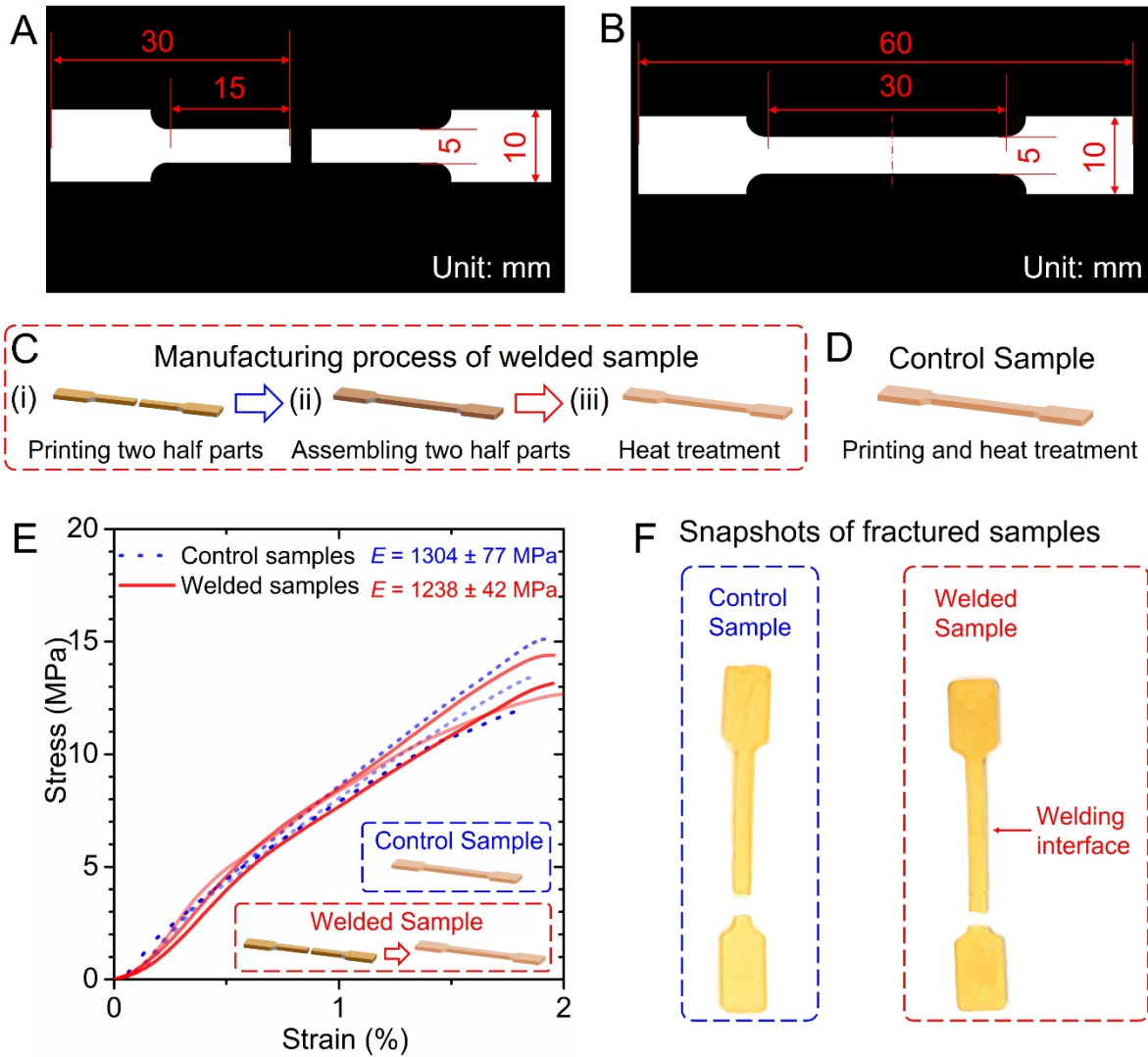

Fig. S20. Design and manufacturing details on the dog-bone samples for uniaxial tensile tests to investigate interfacial bonding. (**A**) Top-view profile dimensions of the welded sample. (**B**) Top-view profile dimensions of control sample. (**C**) Manufacturing process of a welded sample. (**D**) Manufacturing process of a control sample. (**E**) Stress-strain behaviors for both welded and control samples. (**F**) Snapshots of fractured samples.

Supplementary Part 4. Reconfigurable 4D printing of MRC-SMP

Taking the experiment of MRC-SMP with 20 wt.% AUD at an exposure intensity of 1 mW/cm^2 as an example, Fig. S21 shows the method for testing the photorheological properties of MRC-SMPs. The storage modulus and loss modulus of materials were measured on a DHR2 (TA instruments Inc., UK) machine with an aluminum plate geometry (diameter 20 mm, gap 100 μm). First 20 s were detected without light, then 20 s were exposed in 385 nm ultraviolet light with 1, 2, 4, 8 or 16 mW/cm^2 light intensity, and more 20 s were detected after the end of exposure. Aluminum plate rotated at a speed of 5 rad·s^{-1} throughout the 100 s detection process. The intersection of the loss modulus and storage modulus curves is the gel point, and the corresponding time minus 20 s is the curing time.
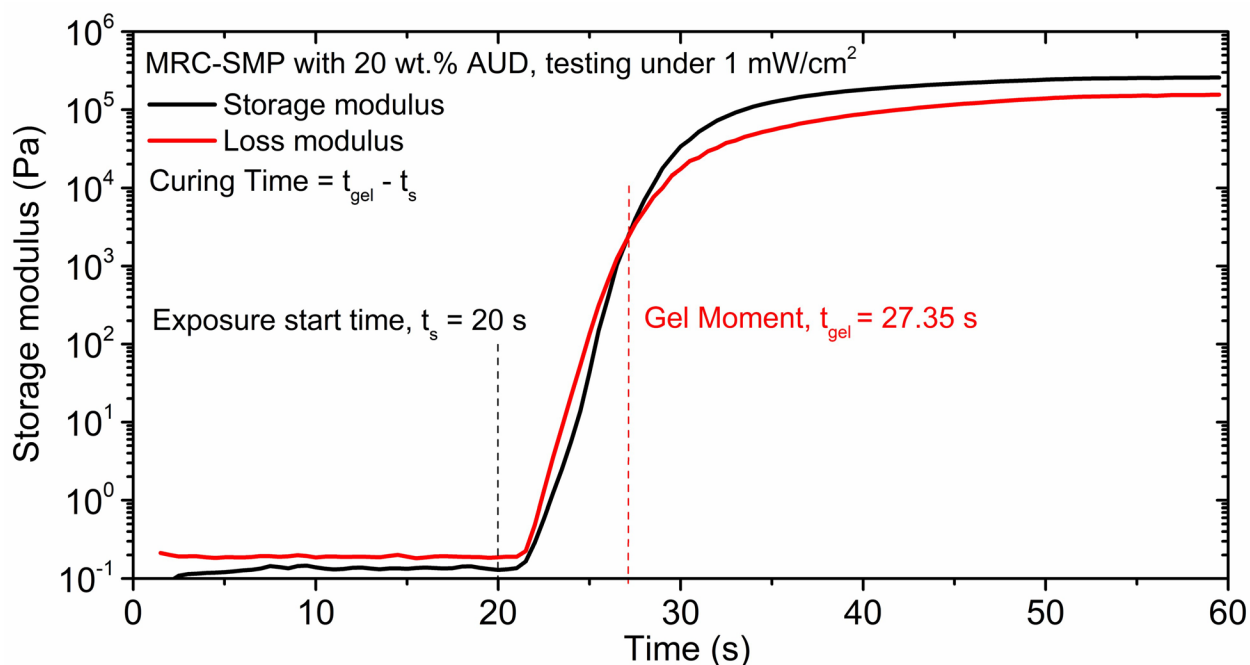

Fig. S21. Curing time test of MRC-SMP with 20 wt.% AUD.

We designed a high heel shoe with a lattice structure heel (Fig. S22A), which has a curved sole and upper that are difficult to print directly. The digital models of the upper and sole are modified to planar models so that they can be 3D printed. Fig. S22B shows the upper, sole, and highly complex heel printed using a DLP printer. By programming the upper and sole, a high heel shoe that matches the shape of the design model can be obtained (Fig. S22C). By program ming the sole and heel (Fig. S22(D to E)) together, a new style of high heel shoe can be obtained (Fig. S22F).
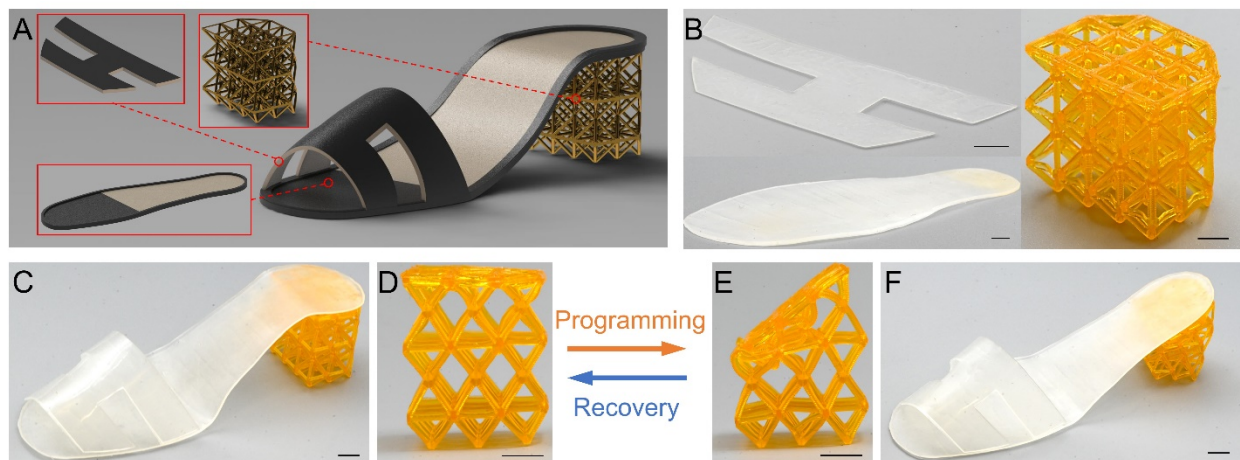

Fig. S22. Demonstrations of design, manufacturing, and SM behavior of a shape-morphing high heel shoe which was 3D printed with MRC-SMP. (**A**) Digital model of additive manufacturing high heel shoe. (**B**) 3D printed upper, sole, and heel. (**C**) A high hell shoe that matches the digital model shape. (**D-E**) Shape memory cycle of the heel. (**F**) A new style of high heel shoe. Scale bar: 5mm.

Fig. S23A shows the detailed dimensions of the MRC-SMP hinge through two sectional views. The length, width, and height of MRC-SMP hinge are 29 mm, 10 mm and 5 mm, respectively. The resistance wire channel is a 1 mm × 1 mm square channel. In Fig. S23B, we conducted three-point bending tests to compare the stiffness of hinges with/without the resistance wire. These tests were conducted on a DMA machine (Q850 DMA, TA Instruments) using a three-point bending fixture with two fulcrums spaced 20 mm apart. The three-point bending tests were conducted at the programming temperature (105°C). The bending displacement of 5 mm was applied to the hinge at a rate of 0.2 mm/s. The addition of resistance wire increases the stiffness of the MRC-SMP hinge from 0.09 N/mm to 0.184 N/mm. The force requires to bending the hinge by 5 mm increases from 0.233 N to 0.568 N after adding the resistance wire.
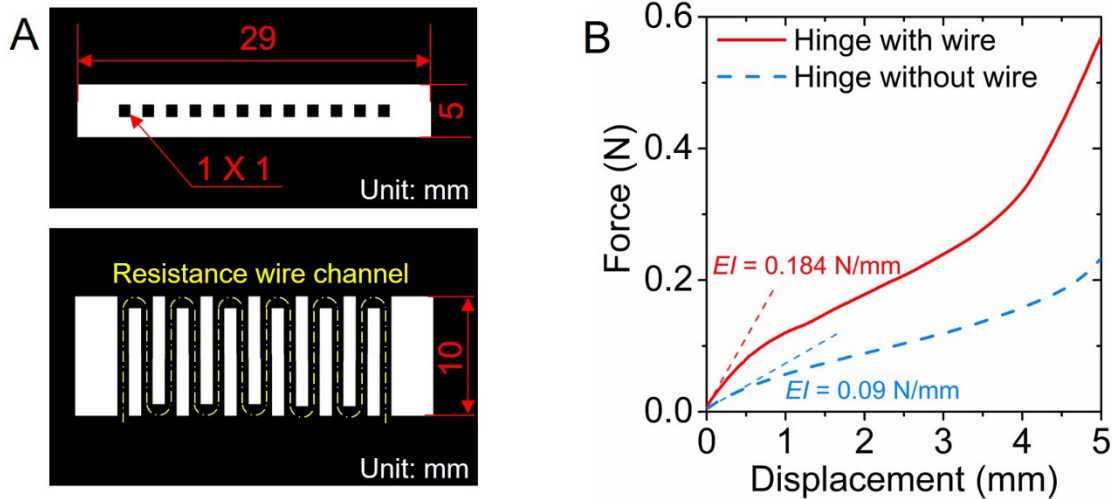

Fig. S23. Three-point bending experiments of electrically-controlled-MRC-SMP hinges. (A) Detailed dimensions of the MRC-SMP hinge. (**B**) Force-displacement curves of three-point bending tests of MRC-SMP hinges.

Fig. S24 shows the thermomechanical properties of the tough polymer used in multi-material printed SM origami. As shown in Fig. S24A, the room temperature modulus of tough polymer is similar to that of MRC-SMP. However, the modulus of tough polymer at high temperatures (778 MPa at 105°C, 107 MPa at 150°C) are much higher than that of MRC-SMP (Fig. 24A), due to its extremely high T_g (156°C) (Fig. 24B) which is much higher than that of MRC-SMP.
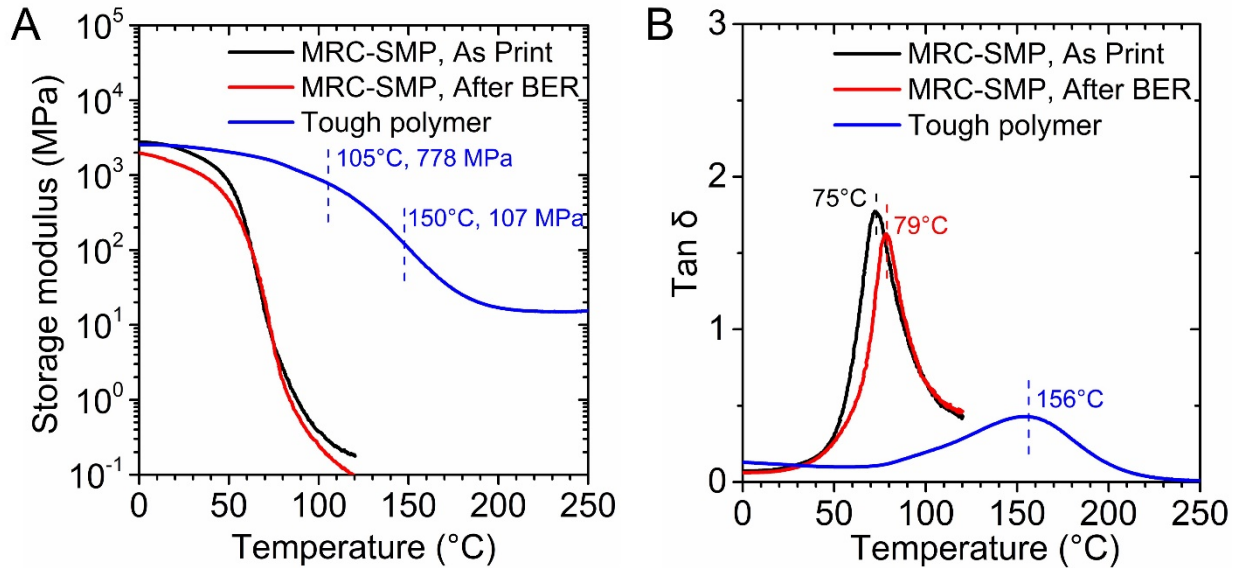

Fig. S24. Thermomechanical properties of MRC-SMP and tough polymer. (**A**) Storage modulus curves. (**B**) Tan δ curves.

Fig. S25A shows the as-prepared samples printed with MRC-SMP, tough polymer and these two materials. Fig. S25B shows the appearance of these samples after BER. The color of MRC-SMP changed from translucent to brown after heat treatment. There is no change in appearance of tough polymer after heat treatment. For multi-materials printing samples, the MRC-SMP in the right half has obvious color change, while the tough polymer in the left half has no change.

As shown in Fig. S25C, in the quasi-static tensile experiment at room temperature, the multi material 3D printed sample fractured at the bonding surface of the two materials, and the material exhibited brittle fracture. After BER, fractures occurred at the necks of the dog bone sample, and the bonding surface in the middle was firmly connected (the right inset in Fig. S25C). The tensile experiment at high temperature (Fig. S25D) also showed that the bonding surface of the two materials underwent bond exchange reaction, forming a robust interface fusion. In the tensile experiment at 105°C and 150°C, the as prepared samples were disconnected from the bonding surface of the two materials (Fig. S25E(i)), and the bonding surface of the after BER samples remained intact (Fig. S25E(ii) - (iii)).
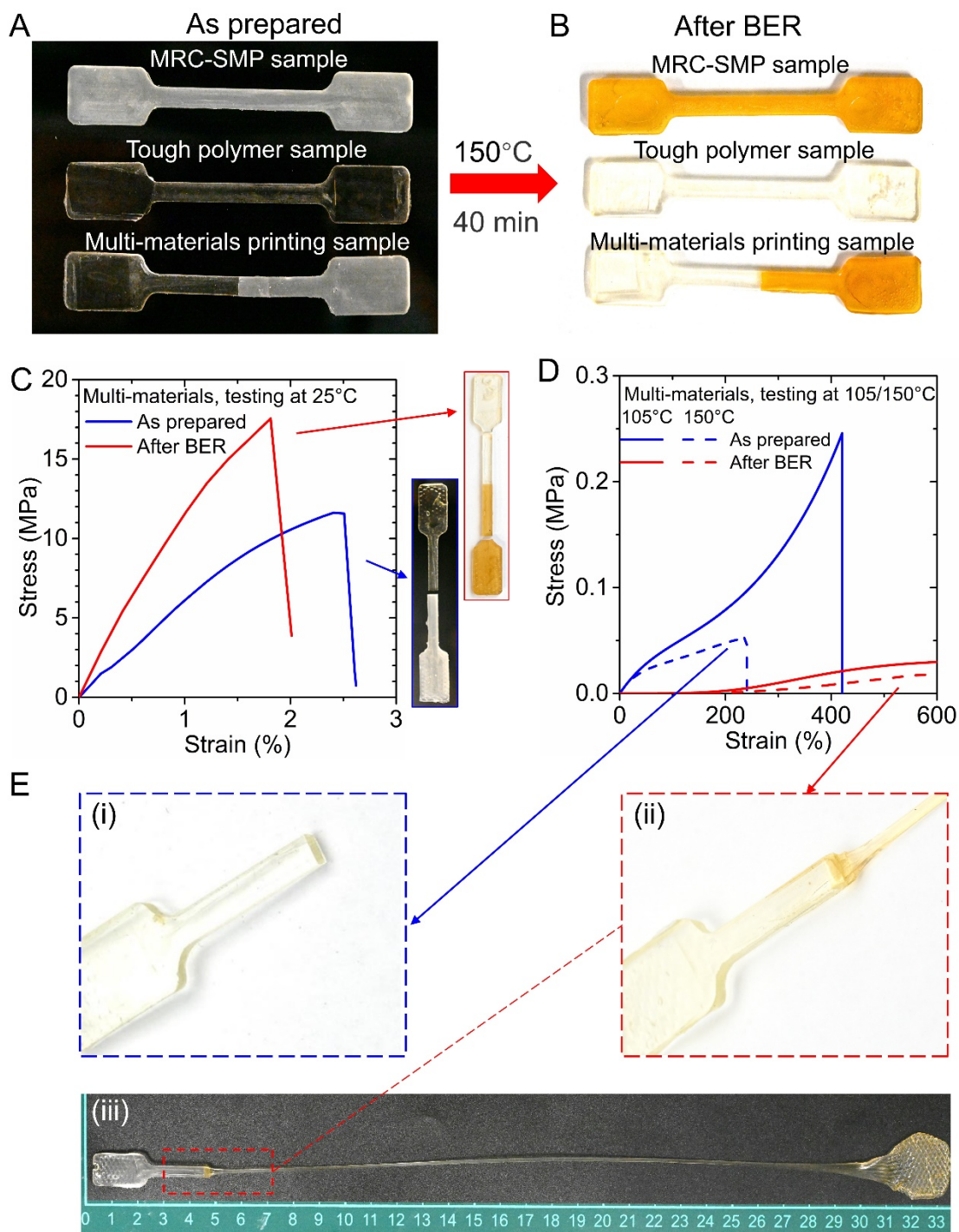
Fig. S25. Mechanical properties of multi-materials 3D printing samples. (**A**) Snapshots of MRC-SMP, tough polymer and multi-materials printed samples (as prepared). (**B**) Snapshots of MRC-SMP, tough polymer and multi-materials samples after BER. (**C**) Mechanical properties of multi-material specimens at room temperature. (**D**) Mechanical properties of multi-material samples at programming temperature and reconfiguration temperature. (**E**) Interface of multi-materials samples after tensile test, (i) as prepared sample, (ii) after BER sample. (iii) Snapshots of the stretched multimaterial sample after BER (the MTS beam reached its maximum height, the samples remained intact).

Legends for movies S1 to S12:

Movie S1: Shape recovery process from flat bridge to flat pattern.

Movie S2: Shape recovery process from flat pattern to flat bridge.

Movie S3: Shape recovery process from flattened arch bridge to arch bridge.

Movie S4: Demonstrations of reconfiguring an MRC-SMP strip with multiple times.

Movie S5: Shape recovery process of a printed MRC-SMP straight lattice structure from highly stretched state to unstretched one.

Movie S6: Shape recovery process of reconfigured MRC-SMP bent lattice structure from highly stretched state to unstretched one.

Movie S7: Shape folding process of an MRC-SMP robotic gripper manufactured by 3D printing, welding and reconfiguration.

Movie S8: Shape recovery process of reconfigured high-heel shoe.

Movie S9: Shape recovery process of the straight hinge from folded state to unfolded one by Joule heating.

Movie S10: Shape recovery process of the reconfigured right-angle hinge from folded state to unfolded one by Joule heating.

Movie S11: Shape recovery process of 3D printed Miura origami from folded state to flatten state.

Movie S12: Shape recovery process of reconfigured Miura origami from fully squeezed state to unsqueezed state.